Journal of The Electrochemical Society

The Electrochemical Society
Advancing solid state & electrochemical science & technology

OPEN ACCESS

The Effect of Doping Process Route on $LiNiO_2$ Cathode Material Properties

To cite this article: Sören L. Dreyer *et al* 2023 *J. Electrochem. Soc.* **170** 060530

View the article online for updates and enhancements.

You may also like

- Reaction Mechanisms of $La_2NiO_{4+\delta}$ Oxygen Electrodes Operated in Electrolysis and Fuel Cell Mode
G. Sdanghi, L. Yefsah, F. Mauvy et al.
- Highly Sensitive and Selective Detection of Diabetic Nephropathy Markers by a Perovskite $LaNiO_{3\delta}$ Based Potentiometric Sensor
Titisha Chakraborty, Munmun Das, Chan Yu Lin et al.
- Effect of Copper-Doping on $LiNiO_2$ Positive Electrode for Lithium-Ion Batteries
Xiang-Ze Kong, Dong-Lin Li, Katja Lahtinen et al.

This content was downloaded from IP address 141.52.248.2 on 04/07/2023 at 09:52

Journal of The Electrochemical Society, 2023 **170** 060530

The Effect of Doping Process Route on $LiNiO_2$ Cathode Material Properties

Sören L. Dreyer,[1] Philipp Kurzhals,[2] Svenja B. Seiffert,[2] Philipp Müller,[2] Aleksandr Kondrakov,[2] Torsten Brezesinski,[1,z] and Jürgen Janek[1,3]

[1]*Battery and Electrochemistry Laboratory (BELLA), Institute of Nanotechnology, Karlsruhe Institute of Technology (KIT), 76344 Eggenstein-Leopoldshafen, Germany*
[2]*BASF SE, 67056 Ludwigshafen, Germany*
[3]*Institute of Physical Chemistry & Center for Materials Research (ZfM/LaMa), Justus-Liebig-University Giessen, 35392 Giessen, Germany*

The pursuit of higher energy density in lithium-ion batteries has driven the increase of the nickel content in lithium nickel cobalt manganese oxide cathode active materials (CAMs), ultimately approaching $LiNiO_2$ (LNO). The downside of the high specific capacity of LNO is more severe degradation of the CAM during battery operation. A common approach to increase structural stability is the introduction of dopants. Various dopants are discussed and compared with each other when integrated into the CAM and tested against undoped materials in the literature, but little attention is given to the role of the process route of their introduction. In this work, we demonstrate with a series of nominally equally Zr-doped LNO samples that effects on various physico- and electrochemical properties are due not to the dopant itself, as one would assume in comparison to an undoped sample, but to the process route and the resulting particle morphology. Dopant, concentration and process routes (co-precipitation, impregnation and co-calcination) were chosen based on their significance for industrial application.
© 2023 The Author(s). Published on behalf of The Electrochemical Society by IOP Publishing Limited. This is an open access article distributed under the terms of the Creative Commons Attribution 4.0 License (CC BY, http://creativecommons.org/licenses/by/4.0/), which permits unrestricted reuse of the work in any medium, provided the original work is properly cited. [DOI: 10.1149/1945-7111/acdd21]

Manuscript submitted April 13, 2023; revised manuscript received May 25, 2023. Published June 20, 2023.

Supplementary material for this article is available online

The increasing demand for lithium-ion batteries with high energy density to power both portable electronics and electric vehicles is met with various research and development efforts to improve the performance from the materials side. As the cathode, and therein mostly the CAM, makes up the largest individual cost and weight contribution, many efforts focus on increasing its capacity.[1] Here, the $LiNi_xCo_yMn_zO_2$ (NCM) material family of layered oxides offers the highest capacities, which increase (for a fixed cut-off voltage) with the nickel content, exemplified by the endmember LNO showing a first-cycle specific discharge capacity above 245 mAh g^{-1}.[2–4] Polycrystalline NCM consists of smaller primary particles aggregated to larger secondary particles and, as some of the authors have recently demonstrated, the particle morphology is the main factor controlling the electrochemical properties.[5–7] Typically obtained from the calcination of $Ni(OH)_2$ and LiOH in the case of LNO or the respective transition-metal hydroxides in the case of NCM, the size of secondary particles depends mostly on the hydroxide precursor CAM (pCAM) particle size, which can be controlled in the precipitation process. At the same time, the size of the primary particles is controlled by the calcination temperature and lithium stoichiometry, the latter also affecting the fraction of Ni^{2+} on the Li-site, often referred to as off-stoichiometry.[5–7]

The main downside of establishing higher capacity (i.e. deeper delithiation) is the reduced structural stability, resulting in faster chemo-mechanical degradation on multiple length scales, i.e. capacity fading.[8,9] For Ni-rich NCM in general and LNO specifically, degradation during cycling is driven by two main phenomena. Firstly, structural rearrangement under loss of lattice oxygen forms a densified, rocksalt-type layer on the particle surface, which hinders lithium diffusion and renders nickel electrochemically inactive (increased share of Ni^{2+} up until approaching NiO stoichiometry).[4,10,11] Secondly, anisotropic unit-cell volume change, especially in the form of the decrease in *c* lattice parameter during the H2/H3 phase transition, leads to the formation of cracks and eventual pulverization of the secondary particles, also exposing additional (reactive) surface area.[3,4,12]

Several strategies have been developed to mitigate CAM degradation both at the particle surface and in the bulk, with coating, doping and morphology modification (i.e. single-crystalline materials) and combinations thereof being most prominent.[13–16] For Ni-rich NCM, various dopants and dopant combinations and their supposed function in performance improvement have been discussed and reviewed in the literature, ranging from elements as light as B to heavier elements like W.[3,4,17] Among the most common dopants are Mg, Al, Ti and Zr, while for LNO also Mn and Co could be considered as dopants.[4,13,15,16]

Depending on dopant and precursor, different process routes are followed to introduce the dopant. The most common are co-calcination of pCAM, lithium source and dopant particles on the one hand,[18–25] and co-precipitation of dopant ions into the pCAM during its preparation on the other hand.[26–39] The impregnation of pCAM with a dopant solution or a suspension of smaller dopant particles and subsequent solvent removal provides a third option, especially if co-calcination leads to insufficient mixing and/or phase separation.[40–51] Despite these and various other process routes being available,[13,15,52–56] comparisons between doped samples obtained from different routes are quite rare,[57,58] as usually comparisons are made with an undoped reference sample. The influence of the dopant on the CAM particle morphology is sometimes discussed in comparisons of doped and undoped samples.[17–19,26,30,41,47,49,50,52,57] Recently, Park et al. demonstrated that, in a series of co-precipitated $LiNi_{0.95}Co_{0.04}X_{0.01}O_2$ (X = one of Al, Ti, Ta, Sb, Nb, W, Mo), the primary particle size strongly depends on the chosen dopant, decreasing with dopant valence state. Furthermore, a linear trend between primary particle size of each doped CAM and capacity fading after 100 cycles was observed.[59] Sun et al. reported a similar finding for $LiNi_{0.90}Co_{0.09}X_{0.01}O_2$ (X = one of Mg, Al, Ti, Ta, Mo), also observing an increase in primary particle aspect ratio with increasing dopant valence.[20] A consideration of the role of the process route on CAM morphology is even rarer,[57] although the latter greatly affects the electrochemical performance.[5–7]

Zirconium has seen widespread use as a dopant for NCM materials and can be introduced into the structure by various routes, including co-calcination,[23–25] impregnation,[46,47,51] and co-precipitation.[26,30,31,39,57] Of note is the diffusion of Zr^{4+} at high temperatures, due to which

[z]E-mail: torsten.brezesinski@kit.edu

doping can also be achieved by heating Zr-coated CAM.[56,60] Vice versa, Zr^{4+} as a dopant is prone to enrich and phase separate at the surface of CAM particles, forming an additional Li_2ZrO_3 phase.[31,51,53,61,62] With this limited bulk solubility in mind, only some studies focused on industrially relevant dopant concentrations, i.e. below 1 mol%.[24,25,47,61,62] The atom position of Zr^{4+} in the structure is not fully understood, with literature reporting localization either in the lithium[63] or transition-metal layer,[23,43] or possibly both.[39,53,64]

Main effects and advantages attributed to the dopant include increased *c* lattice parameter, faster lithium diffusion, smoother H2/H3 phase transition, less volume change during delithiation, less crack formation and reduced surface-layer formation, ultimately resulting in longer cycle life, improved rate capability, reduced impedance and less polarization of the CAM.[23,24,31,47,56,60,62,65] At high state of charge (SOC), zirconium was shown to suppress charge transfer to oxygen, thereby reducing the loss of lattice oxygen and subsequent gas evolution.[46] In some studies, a difference in CAM particle size or morphology between doped and undoped material was observed and partially related to altered properties.[25,26,30,47,57]

In this article, we demonstrate on a series of 0.25 mol% Zr-doped LNO obtained from three different process routes, namely co-calcination, impregnation and co-precipitation, that not the dopant but the process route leads to a difference in physico- and electrochemical properties, especially considering primary particle morphology. The rather low dopant concentration is chosen due to its industrial relevance, i.e. the redox-active metal content remains high and the redox-inactive dopant concentration low for maximum energy density. Furthermore, a phase separation is avoided as much as possible, as the Zr^{4+} fraction is low enough to mostly remain in the bulk LNO.

Experimental

Doping and calcination.—Calcination of undoped LNO was performed as described in the literature[5] using a commercial $Ni(OH)_2$ precursor (d_{50} = 4 μm, Hunan Zoomwe Zhengyuan Advanced Material Trade Co., Ltd., China) and $LiOH{\cdot}H_2O$ (Albemarle Germany GmbH, Germany). In short, precursors were blended (1.02 mol eq. $LiOH{\cdot}H_2O$ per 1.0 mol eq. $Ni(OH)_2$) and calcined under O_2 flow (100 l h^{-1}, equal to about 10 furnace volume exchanges/h) in a box furnace (Linn High Term GmbH, Germany) at 400 °C for 4 h, then at 700 or 750 °C for 6 h, with intermediate heating ramps of 3 °C min^{-1}. Samples were cooled down to 120 °C and transferred to dry room atmosphere (21 °C, dew point < −40 °C) with minimal exposure to ambient air. The obtained powders were sieved (32 μm mesh) prior to further processing and characterization. Co-calcined Zr-doped LNO was obtained in the same way, but with the addition of ZrO_2 (Daiichi Kigenso Kagaku Kogyo Co., Ltd., Japan) to the blend (0.9975 mol eq. $Ni(OH)_2$, 0.0025 mol eq. ZrO_2, 1.02 eq. $LiOH{\cdot}H_2O$). To obtain Zr-impregnated pCAM, $Ni(OH)_2$ was dispersed in water (1:1 by weight), and a suspension of 20 wt% colloidal ZrO_2 nanoparticles (Nyacol Nano Technologies, Inc., USA) in water, stabilized with ammonia, was added dropwise under stirring. The solvent was removed at 120 °C in a vacuum overnight, and the obtained powder was heated to 500 °C for 3 h in the box furnace under O_2 flow, then transferred to the dry room and sieved as described above. To obtain LNO, the Zr-doped/coated NiO was blended with 1.02 mol eq. $LiOH{\cdot}H_2O$ and calcined as described above. Co-precipitated, 0.25 mol% Zr-doped pCAM (d_{50} = 4 μm) was obtained from Hunan Zoomwe Zhengyuan Advanced Material Trade Co., Ltd., China and calcined with 1.02 mol eq. $LiOH{\cdot}H_2O$ (per 0.9975 mol eq. $Ni(OH)_2$). In a variation, the doped pCAM was pre-dried similar to impregnated pCAM at 500 °C for 3 h before being blended with $LiOH{\cdot}H_2O$ and calcined as described above.

PXRD.—Synchrotron powder X-ray diffraction (PXRD) measurements were performed, in analogy to a previous work,[5] at the ALBA synchrotron BL04-MSPD beamline at a wavelength of λ = 0.62001 Å (calibrated using a Si NIST standard) using a Si 111 monochromator and a MYTHEN position sensitive detector in 2-theta angular range of 2°–82°. Samples were measured in flame-sealed borosilicate capillaries of 0.7 mm diameter and mounted on a spinning sample holder. Data were collected in Debye–Scherrer geometry for 27 different positions of the detector, with a data acquisition time of 30 s for each position. Rietveld refinement was performed using the FullProf software package, based on a hexagonal α-$NaFeO_2$ structure with *R*–3m space group. The instrumental broadening was determined by measuring a NAC ($Na_2Ca_3Al_2F_{14}$) standard in the same sample configuration. The model used for the fitting is based on Thompson-Cox-Hastings pseudo-Voigt convoluted with axial divergence asymmetry functions. Sample contribution to peak broadening was determined by the instrumental resolution function, so that a volume-averaged value of the crystallite size was obtained via the Scherrer equation. Refinement of the parameters of the structural model was done for consecutive iteration cycles until convergence was reached, and the quality of fit was checked by inspection of the R_{wp} (weighted profile factor with all non-excluded points), R_{Bragg} (Bragg *R*-factor) and χ^2 (reduced chi-square). In an initial LeBail fit, two asymmetry parameters were refined and held constant during subsequent Rietveld refinement. For all samples, in the final iteration, 12 parameters were refined: scale factor, zero shift, *a* and *c* lattice parameters, U, X, Y as parameters of the Gaussian (U) and Lorentzian (X, Y) contribution to the pseudo-Voigt function, fractional atomic coordinate of oxygen z_{ox}, occupancy of Ni^{2+} on the Li-site (assuming site remains fully occupied) and B_{iso} (isotropic displacement parameter) of O, Ni and Li.

Electron microscopy.—Scanning electron microscopy (SEM) was performed using an Ultra 55 (Carl Zeiss AG, Germany) microscope equipped with a thermal field-emission cathode and an Everhart-Thornley secondary electron detector at an operating voltage of 5 kV. Powder samples were fixed on conductive carbon cement (Plano GmbH, Germany) and a 6 nm Pt layer was added via sputter deposition (SCD 500 Sputter Coater, BalTec AG, Switzerland). Automated image segmentation was used to obtain the equivalent diameter of the primary particles from SEM images at 20 k magnification, as described previously.[6] At least 10 images per material were segmented.

Samples for transmission electron microscopy (TEM) were prepared by broad ion-beam milling using a Jeol (Jeol Ltd., Japan) Ar-ion slicer (EM-09100 IS) and/or focused ion beam milling using a Helios G4 machine (Thermo Fisher Scientific Inc., USA). The samples were imaged using a Tecnai Osiris (Thermo Fisher) operated at 200 kV and a Themis Z3.1 (Thermo Fisher) equipped with a probe-corrector operated at 300 kV both under high-angle annular dark-field scanning TEM (HAADF-STEM) conditions. Chemical composition maps were acquired by energy-dispersive X-ray spectroscopy (EDS) with integrated SuperX G1 and G2 detectors. Elemental maps were evaluated with the Esprit (version 2.1, Bruker, USA) and Velox 3 (Thermo Fisher) software.

Acid titration.—Residual LiOH and Li_2CO_3 in the LNO samples were determined by stirring a suspension of 2 g of CAM in 10 ml deionized water for 20 min under N_2 atmosphere in a glovebox and titrating the solution resulting after filtration through a syringe filter with 0.1 M HCl solution (Bernd Kraft GmbH, Germany). To this end, a Titrando 808 automatic titrator (Deutsche Metrohm GmbH & Co KG, Germany) and a glass pH electrode (Metrohm) were used. Two separate equivalent points were observed and used to distinguish between LiOH and Li_2CO_3, with hydroxide and carbonate ions being protonated first and the resulting bicarbonate being protonated again later.

ICP-OES.—0.3 g of CAM was digested in 5 M HCl under stirring and gentle heating. The solution was diluted with deionized water, and the concentrations of Ni, Li and Zr were measured with an

Agilent 5100 inductively coupled plasma-optical emission spectroscopy (ICP-OES) device (Agilent Technologies Inc., USA). For each sample, three individual measurements were performed.

LA-ICP-MS.—For single particle analysis using laser ablation-inductively coupled plasma-mass spectrometry (LA-ICP-MS), a 193 nm ArF excimer laser (NWR193 ablation system, Elemental Scientific Lasers, USA) equipped with a two-volume cell (Two Vol2 ablation cell, Elemental Scientific Lasers) was coupled to an ICP-MS (8900 ICP-MS Triple Quad, Agilent Technologies, USA). The samples were transported in a carrier gas flow (He, 850 ml min^{-1}) and introduced via a dual concentric injector (Elemental Scientific Lasers) to the ICP-MS. An additional gas flow (Ar, 1 l min^{-1}) was added and the sample transferred via a quartz injector pipe (2.5 mm inner diameter) into the plasma. The ICP-MS was equipped with a Pt sampler and skimmer. To reduce polyatomic interferences, it was operated in single quadrupole-kinetic energy discrimination mode adding He as collision gas. The RF coil was set to 1300 W, and the setup was tuned daily for maximum signal intensity and an oxide ratio (m/z:m/z = 232:248) below 0.8% with a NIST glass standard (NIST SRM 612). The samples were ablated with single spots and a laser pulse frequency of 100 Hz. A laser energy of 1.5 J cm^{-2} and 80 bursts ensured complete ablation of each particle. For each measurement, at least 200 particles were ablated. Additionally, the background of the carbon cement tab was tested. The ICP-MS was operated in time-resolved analysis mode, and for each element one isotope ($^{61}Ni^{+}$ and $^{90}Zr^{+}$) was detected with a dwell time of 100 μs. The short dwell time enabled the collection of >50 data points per particle, even for the smallest particles. Data evaluation was carried out using RStudio and a homemade script. Particle event integration was triggered by crossing a manually chosen peak trigger value and ended after a manually chosen timeframe (1 s). As nearly all background signals were 0 counts, the integrated particle events were not corrected.

Elemental analysis of carbon content.—In a single-use ceramic cup, 200 mg of pCAM was mixed with 500 mg of iron granulate, and the mixture was covered with 1.5 g of tungsten granulate. The sample was heated in a flow of pure O_2 in the induction furnace of the analyzer (Eltra CS 800, Eltra GmbH, Germany), and the released CO_2 was quantified via infrared spectroscopy.

Cathode preparation.—Electrodes for electrochemical characterization were prepared by mixing the CAM powders with Super C65 conductive carbon (Imerys Graphite & Carbon, Switzerland) and PVDF binder (Solef 5130, Solvay GmbH, Germany) in a 94:3:3 mass ratio. For this, a 7.5 wt% binder solution in N-methyl-2-pyrrolidone (NMP, BASF SE, Germany) was mixed with additional NMP and the conductive carbon for at least 24 min at 2000 rpm using an ARE 250 planetary mixer (Thinky Corporation, Japan). The CAM powder was added to the obtained slurry and mixed for additional 10 min. The solid fraction of the final slurries was 61 wt%. The slurries were cast onto 20 μm Al foil (Nippon Light Metal Co., Ltd., Japan) using a box-type coater (110 μm wet-film thickness, 6 cm width, Erichsen GmbH & Co. KG, Germany) and an automated coating table (5 mm s^{-1}, Coatmaster 510, Erichsen GmbH & Co. KG, Germany). The coated tapes were placed in a vacuum oven (VDL 23, Binder GmbH, Germany) and dried at 120 °C in a dynamic vacuum for 12 h. The cathode tapes were then compressed using a CA5 calendar (Sumet Systems GmbH, Germany) at a set line force of 30 N mm^{-1} and a roller speed of 0.5 m min^{-1}. The active material loading was 9 (±0.5) mg cm^{-2} and the electrode density was 3.0 (±0.2) g cm^{-3}.

Cell preparation.—For coin half-cells, circular electrodes with a diameter of 14 mm were punched out using a high-precision handheld punch (Nogamigiken Co., Ltd., Japan). After weighing, the electrodes were transferred to an Ar-filled glovebox for assembly of CR2032 coin cells (Hohsen Corp, Japan). To the cathode, a 17 mm diameter GF/D glass fiber separator (VWR International GmbH, Germany), a 15.8 mm diameter Li-metal anode (Shandong Gelon LIB Co., Ltd., China) and 95 μl LP57 electrolyte (1 M $LiPF_6$ in ethylene carbonate:ethyl methyl carbonate 3:7 by volume, BASF SE, Germany) were added, and the cells were sealed by crimping with an automated crimper (Hohsen Corp.). Single-layer pouch full cells were assembled in dry-room atmosphere from 40·20 mm^2 cathodes, 50·30 mm^2 microporous separators (Celgard 2500, Celgard, LLC, USA), 42·22 mm^2 graphite anodes (7 mg cm^{-2} loading) and 500 μl LP472 electrolyte (1 M $LiPF_6$ in ethylene carbonate:diethyl carbonate 3:7 by volume, with 2 vol% vinylene carbonate, BASF SE, Germany). The n/p ratio[66] was calculated based on the first-cycle specific capacity in half-cells (250 mAh g^{-1} for LNO, 330 mAh/g for graphite). With a graphite loading of 64 mg per anode and LNO loadings between 69 and 73 mg per cathode (8.6 to 9.1 mg cm^{-2}), n/p ratios of 1.16–1.22 were obtained.

Electrochemical testing.—Coin half-cells were cycled at 25 °C between 3.0 and 4.3 V vs Li^{+}/Li using a battery testing system (Series 4000, MACCOR, USA). Assuming 1 C as 200 mA g^{-1}, the applied current was equal to C/20 in the first two cycles and C/3 in the following cycles, with the exception of a rate test with one cycle each at C/3, C/10, 1 C and 2 C. Additional coin half-cells were cycled to determine the specific capacitance according to a recently presented method.[67] Cells were cycled between 2.5 and 4.3 V, while at the end of discharge an additional constant-voltage step was implemented (until the current was lower than C/250) to ensure the presence of blocking conditions. Then, an alternating current (C/50 amplitude, 100 mHz frequency, 20 periods duration) was modulated onto the discharge current. By fitting the current and voltage response to sine functions, the specific capacitance can be calculated from the phase shift, as demonstrated elsewhere.[67–69] Pouch full cells were cycled between 2.8 and 4.2 V at a rate of C/10 in the first two cycles and then at C/3 for 10 cycles. A rate test at C/3 charge and two cycles each at 0.5 C, 1 C, 2 C and 3 C discharge was implemented and subsequently repeated after every 100 cycles at C/3 rate.

DEMS.—For gas analysis via differential electrochemical mass spectrometry (DEMS), a custom-built cell containing a 30 mm diameter cathode with a 4 mm diameter hole in the center, a 40 mm diameter GF/D separator, a 32 mm diameter Li-metal anode and 800 μL LP57 electrolyte was cycled at 0.1 C rate between 3.0 and 4.3 V, while a constant 2.5 ml min^{-1} stream of He carrier gas (purity 6.0) was passed through the cell. The extracted gas mixture was analyzed with a mass spectrometer (GSD320, Pfeiffer Vacuum GmbH, Germany). For CO_2 quantification, a calibration was carried out using gas with 100 ppm CO_2 content. Further details can be found elsewhere.[70–72]

Results and Discussion

Precursors.—For the synthesis of undoped LNO and LNO doped via co-calcination and impregnation, a batch of spherical $Ni(OH)_2$ pCAM (d_{50} = 4 μm) with rod-like primary particles, as shown in Figs. S1a and S1b, was used. Figures S1c and S1d show the pCAM after impregnation with ZrO_2 nanoparticles and subsequent heating during which the $Ni(OH)_2$ is converted to NiO. In the following, this procedure is referred to as pre-drying ("predr." in figures), wherein full conversion was ensured by subsequent ICP-OES analysis revealing a composition of >77.5 wt% Ni, in contrast to ~64% for the initial $Ni(OH)_2$. The presence of fragmented pCAM particles is likely due to deagglomeration and sieving of the thus obtained NiO. Since also during LNO synthesis, the conversion of $Ni(OH)_2$ to NiO occurs already below 300 °C, prior to the onset of lithiation, no large change in reactivity is expected when employing NiO instead of $Ni(OH)_2$ as pCAM as long as particle morphology is conserved.[73,74] The Zr-containing, co-precipitated pCAM of equal size (d_{50} = 4 μm) is shown in Figs. S1e and S1f. It was surprisingly

found by elemental analysis that the co-precipitated pCAM contained more carbon than the regular pCAM, as detailed in Table S1. To reduce the carbon content, in one variation, the co-precipitated ("co-prec." in figures) pCAM was subjected to the same heating procedure in O_2 by which the impregnated pCAM was pre-dried, thereby oxidizing organic residues to CO_2 and converting $Ni(OH)_2$ to NiO. The resulting pCAM is shown in Figs. S1g and S1h. Probable sources of the residues are the use of organic complexing agents such as citric acid or lactic acid, the use of metal acetates as precursors in the precipitation reaction or base solution being exposed to atmospheric CO_2 before or during precipitation.[57,65,75,76]

The dopant distribution in the Zr-containing pCAMs was analyzed via STEM-EDS, as shown in Fig. S2. Impregnation resulted in the formation of a surface coating-like zirconium layer on the secondary particles, and there are no large agglomerates outside of the pCAM. Between secondary particles, Zr^{4+} seems evenly distributed, but the content within the particles is too close to the detection limit to be discussed quantitatively from EDS. Co-precipitated pCAM also shows Zr^{4+} to be evenly distributed between and within secondary particles, yet in the non-pre-dried pCAM particulate zirconium enrichment was observed in one case. No such enrichment was evident after pre-drying.

Composition and crystal structure.—Table I summarizes the composition of the 10 LNO samples discussed in this work according to ICP-OES and acid titration. As expected, a high content of Li_2CO_3 was found in the co-precipitated sample after calcination. Li_2CO_3 and LiOH are common impurities formed by residual lithium upon contact with CO_2 and H_2O in air.[77,78] The excess carbonate, however, was formed during calcination by the decomposition of organic residues in the pCAM (in the presence of lithium), since it is not observed for the other LNO samples, which were handled in the same way and the carbon source was already present in the pCAM. A fifth set of LNO was thus prepared from the pre-dried, co-precipitated pCAM.

PXRD patterns (see Figs. S3 and S4) of each sample confirm the LNO structure and additionally show the presence of aforementioned Li_2CO_3 impurities (see Figs. S5 and S6) for the co-precipitated samples. Rietveld refinement was performed to determine the unit-cell volume, apparent crystallite size and off-stoichiometry, with the results shown in Table II. As expected, a clear trend is observed between calcination temperature and crystallite size for all samples, as reported previously.[5,6] A slight increase in off-stoichiometry is also observed with increasing calcination temperature, except for the LNO obtained from co-precipitated pCAM. The higher off-stoichiometry in these materials is explained by the formation of Li-containing impurities. While Zr-doping is reported to increase the c lattice parameter and therefore the unit-cell volume,[26,43,46,53,60,65] the effect is likely overshadowed in this study due to the low chosen concentration and the also present effect of off-stoichiometry. At the same time, the low concentration of Zr^{4+} did not allow for inclusion of its position and occupancy in the refinement, which might explain the slightly lower quality of fit when compared to LNO from a previous report characterized under the same measurement conditions.[5]

Particle morphology.—SEM images of the different LNO particles calcined at 700 °C are shown in Fig. 1a. It is evident that the shape and size of primary particles are highly dependent on the chosen process route, while the secondary particle morphology and size were hardly affected. The primary particle size distribution determined by automated image segmentation[6] is shown in Fig. 1b and is in good agreement with the crystallite size obtained from PXRD.

No discernible difference in primary particle size is observed between undoped and co-calcined material, while LNO obtained from impregnated and non-pre-dried, co-precipitated pCAM is composed of smaller primary particles, with a large share of <200 nm particles. On the other hand, the pre-dried, co-precipitated pCAM resulted in larger primary particles compared to all other samples. It has previously been reported that Zr^{4+} doping is associated with reduced primary particle size,[47] as are other dopants, mostly of higher valence state.[20,49,50,59] The observed restriction of grain growth can be explained by a dopant-induced change in surface energy, including segregation of dopant along grain boundaries.[17,59] This is not limited to battery materials, but can be applied to the sintering of ceramics in general.[79,80]

Since in this work all LNO samples are doped by nominally equal amounts of Zr^{4+}, the difference in primary particle size must be connected to the process route by which zirconium was provided. During the synthesis, first the incorporation of lithium into the rocksalt structure of NiO and later the formation of LNO occur already at lower temperatures such as the herein applied hold at 400 °C, or during ramp up to the final calcination temperature, which is then held mostly to allow for layer formation, i.e. reduction of the amount of Ni^{2+} on the Li-site, and particle growth.[73,74] Assuming the role of Zr^{4+} as grain growth-reducing dopant and considering Fig. S2, a possible explanation for the difference in particle size is the initial distribution of Zr^{4+}. In case of impregnation, zirconium is already present at the grain boundaries, while in co-precipitated material, it has to diffuse from the bulk to the grain boundaries, and in case of co-calcination, from the ZrO_2 precursor to the CAM particles. In studies using the conversion of a ZrO_2 coating to achieve doping, diffusion of Zr^{4+} into the bulk was only observed at temperatures around 700 °C.[56,60]

For the non-pre-dried, co-precipitated material, the carbon-based impurity likely aided in Zr^{4+} diffusion or was an active segregant itself. Figure S7 shows the obtained particles and their size distribution for a final calcination temperature of 750 °C. Again, the crystallite size from PXRD refinement is in good agreement with the average primary particle size determined from image segmentation.[6] At higher temperature, faster Zr^{4+} diffusion and particle growth as well as change in Zr^{4+} solubility[64] alleviated the effect of dopant, with only the carbon-contaminated, co-precipitated pCAM yielding smaller primary particles.

Table I. ICP-OES and acid titration results.

LNO sample	Calcination temperature ϑ/ °C	Zr/(Ni+Zr)/mol%	Li_2CO_3/wt%	LiOH/wt%
Undoped	700	n.a.	0.59	0.93
	750	n.a.	0.51	0.49
Co-calcination	700	0.22	0.58	1.02
	750	0.22	0.57	0.50
Impregnation	700	0.22	0.45	1.01
	750	0.22	0.37	0.64
Co-precipitation	700	0.26	1.37	1.19
	750	0.26	1.22	0.51
Co-precipitation (pre-dried)	700	0.26	0.40	0.86
	750	0.26	0.36	0.68

Table II. Rietveld refinement results. Ni_{Li} describes Ni^{2+} occupancy on the Li-site and R_{Bragg} and χ^2 indicate the goodness of fit.

LNO sample	Calcination temperature ϑ/ °C	Crystallite size/nm	Unit-cell volume/Å^3	Ni_{Li}/%	R_{Bragg}	χ^2
Undoped	700	242	101.793	2.5	3.06	63.2
	750	512	101.829	3.2	2.64	95.3
Co-calcination	700	194	101.821	2.6	2.28	95.7
	750	454	101.841	3.4	2.38	93.1
Impregnation	700	183	101.711	2.2	2.41	83.1
	750	498	101.742	2.7	2.95	141.0
Co-precipitation	700	211	101.940	3.1	2.40	115.0
	750	352	101.958	3.0	2.31	121.0
Co-precipitation (pre-dried)	700	293	101.667	2.9	2.82	98.4
	750	672	101.723	2.8	3.09	124.0

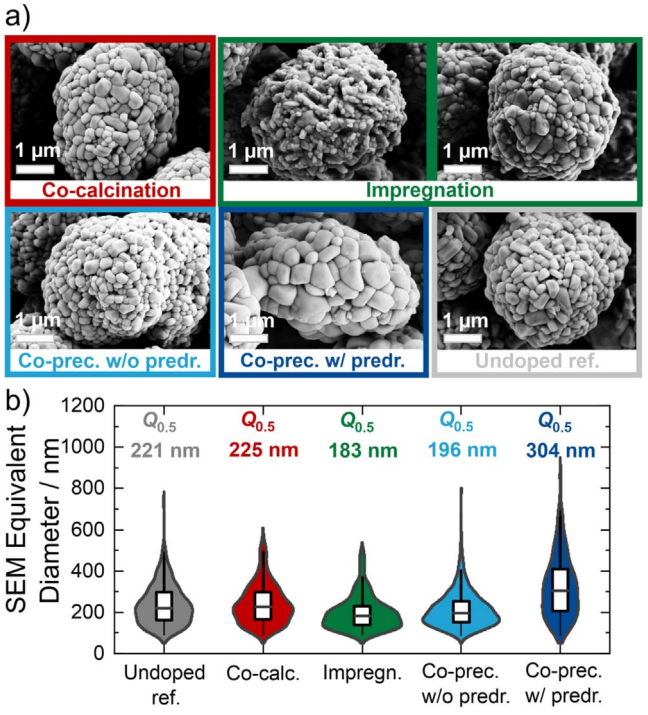

Figure 1. Dependence of (a) particle morphology and (b) size on process route for LNO calcined at 700 °C.

Dopant distribution after calcination.—The distribution of dopant both within and between secondary particles in dependence of the chosen process route is elucidated via STEM-EDS and LA-ICP-MS, as shown in Figs. 2a–2d and 3a–3d for all samples calcined at 700 °C. While EDS provides high-resolution images of the Zr^{4+} distribution within secondary particles, statistical evaluation and interparticle comparisons are difficult. On the other hand, LA-ICP-MS delivers the interparticle-dependent relative distribution and allows for statistical evaluation due to a high number of sampled secondary particles.[81,82] Particle or area-resolved ICP techniques have previously found applications in the battery context, for example in the study of NCM classification[83] and subsequent SOC heterogeneity,[84] transition-metal deposition on anodes[85] and local solid-electrolyte composition.[86]

Using EDS, it was found that all process routes result in an enrichment of zirconium at grain boundaries, as it was presumed in the previous section and is in accordance with literature reports.[31,51,53,61,62] The concentration within the primary particles is too close to the detection limit to be discussed quantitatively, but all primary particles appear to contain a rather similar concentration of Zr^{4+}. Only in LNO stemming from pre-dried, co-precipitated pCAM, a separation of small Zr-rich grains was observed in a few particles, see Fig. 2d. Similar observations, albeit with slightly less apparent grain-boundary enrichment, were made for the samples calcined at 750 °C (see Fig. S8).

Via LA-ICP-MS, the relative composition of individual secondary particles can be determined, here shown in a comparison of Zr and Ni counts. The absolute count number of Ni is directly proportional to the particle mass (i.e. to the cube of particle size), so that a high linearity between absolute Zr count and absolute Ni count indicates a uniform interparticulate Zr^{4+} distribution.[81,87,88] While all process routes lead to a rather uniform distribution of Zr^{4+} between secondary particles, co-precipitation without pre-drying gave an especially narrow dopant distribution. Outliers are visible in Fig. 3d and support the observation of separated, Zr-rich grains as discussed for Fig. 2d. At a calcination temperature of 750 °C, the distribution of Zr^{4+} between secondary particles became much broader for all process routes, i.e. more inhomogeneous, as shown in Fig. S9.

Electrochemical properties.—Having established the particle and dopant properties, all materials were tested electrochemically. Figure 4a shows the discharge capacity of coin half-cells (referred to as CHC) over 56 cycles for the LNO samples calcined at 700 °C. Even in the first two cycles at a rate of C/20, a difference of up to 10 mAh g^{-1} depending on the chosen process route is evident, with LNO obtained from impregnated pCAM delivering the highest (250 mAh g^{-1}) and LNO from pre-dried, co-precipitated pCAM delivering the lowest specific capacity (240 mAh g^{-1}). After a rate test and 50 cycles at C/3, this difference increased to 25 mAh g^{-1}, with LNO obtained from impregnated pCAM again delivering the highest (180 mAh g^{-1}) and LNO from pre-dried, co-precipitated pCAM delivering the lowest specific capacity (155 mAh g^{-1}). Undoped LNO, co-calcined LNO and LNO from non-pre-dried, co-precipitated pCAM all showed very similar performance, with 166 mAh g^{-1} remaining after cycling.

The initial difference in specific capacity, a consequence of the first-cycle irreversibility, was previously shown to be determined by primary particle size,[6,7,89] wherein smaller particles result in a larger interface area between CAM and electrolyte. This interface area was monitored in situ by the capacitance method of Oswald et al.,[67–69] with the resulting specific capacitance shown in Fig. 4b. Before cycling, all materials show similar capacitance values, in good agreement with the finding that the specific capacitance of pristine CAM is largely determined by the secondary particle size (specific surface area).[6] The only exception is a slightly higher specific capacitance of LNO obtained from non-pre-dried, co-precipitated pCAM. Since this material contains a higher amount of surface impurities, the difference may be explained by the exposure of fresh surface after their partial decomposition/dissolution into the electrolyte, similar to the effect of washing discussed in the literature.[6] In the following 4–5 cycles, an increase to an individual level is observed for all materials, with the capacitance then remaining close to this maximum level in the following cycles. The increase is due to particle fracture upon cycling, enabling the inner pore network of the

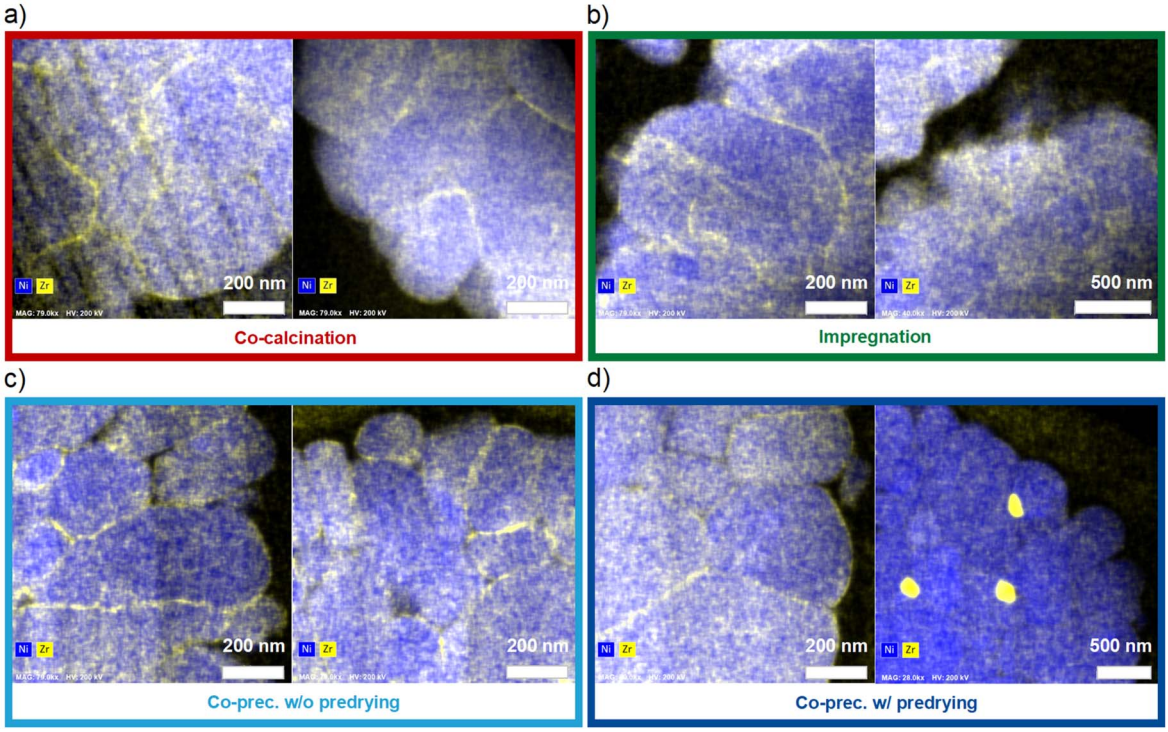

Figure 2. STEM-EDS investigation of Zr^{4+} distribution in secondary particles of LNO calcined at 700 °C. Ni is mapped in blue, Zr in yellow.

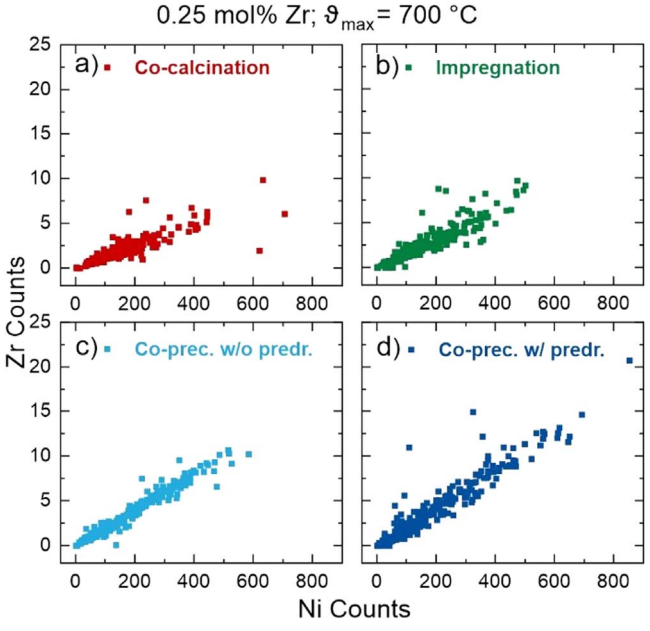

Figure 3. LA-ICP-MS investigation of Zr^{4+} distribution between secondary particles for LNO samples calcined at 700 °C.

secondary particles to be penetrated by electrolyte. The maximum value for each material is determined by the primary particle size, with smaller particles as those obtained from impregnated or non-pre-dried, co-precipitated pCAM resulting in higher capacitance because of their larger specific surface area. It is this surface area and specific capacitance that has been shown to determine both the first-cycle capacity loss and long-term cycling performance due to reduced kinetic hindrance of lithium intercalation at the end of discharge.[6]

For LNO from either impregnated or non-pre-dried, co-precipitated pCAM, the two materials with the smallest primary particle size and therefore largest capacitance, the same maximum value (0.69 F g^{-1}) is obtained. However, both a distinct difference in the increase of capacitance and a difference in cycling performance are found, suggesting these observations to be correlated. For LNO from non-pre-dried, co-precipitated pCAM, a rapid increase in capacitance, especially after just one cycle, is observed and the maximum value reached after five cycles. It can be assumed that the rapid capacitance increase is again due to the presence of surface impurities, which upon decomposition/dissolution during the first charge reveal previously covered surface and blocked pores. However, this also leads to further side reactions such as electrolyte degradation, which likely contributes to the lower cycling performance in comparison to the sample prepared by impregnation. At the same time, for LNO from impregnated pCAM a slower, continuous increase until the 12th cycle is observed. A possible explanation is a slower crack-formation process due to the previously discussed Zr-rich grain boundaries acting as a protective coating, while the beneficial kinetics resulting from the smaller primary particles still leads to greater specific capacities. The data for LNO calcined at 750 °C, where larger particle size reduced the electrochemical performance and specific capacitance, are shown in Fig. S10.

In various studies, it has been shown that a higher capacity retention of doped material correlates with a smaller particle or grain size relative to undoped material achieved by modification with high valence dopants.[20,49,50,59] In these cases, the smaller particle size resulted from dopant-induced grain growth suppression. In this work, a similar performance dependency on particle size is observed and especially clear in the comparison of impregnated and co-calcined LNO, while the surface impurities and their presence, respectively removal, may additionally affect the performance of co-precipitated LNO. Nevertheless, the observation of different primary particle sizes in nominally equally doped CAM depending on the process route, in combination with no difference in particle size and performance between co-calcined and undoped LNO, means that the route of dopant introduction, and not the sole addition of dopant, is at the root of performance improvement.

For the samples calcined at 700 °C, further characterization was performed. Figure 5a shows the discharge capacity of pouch full

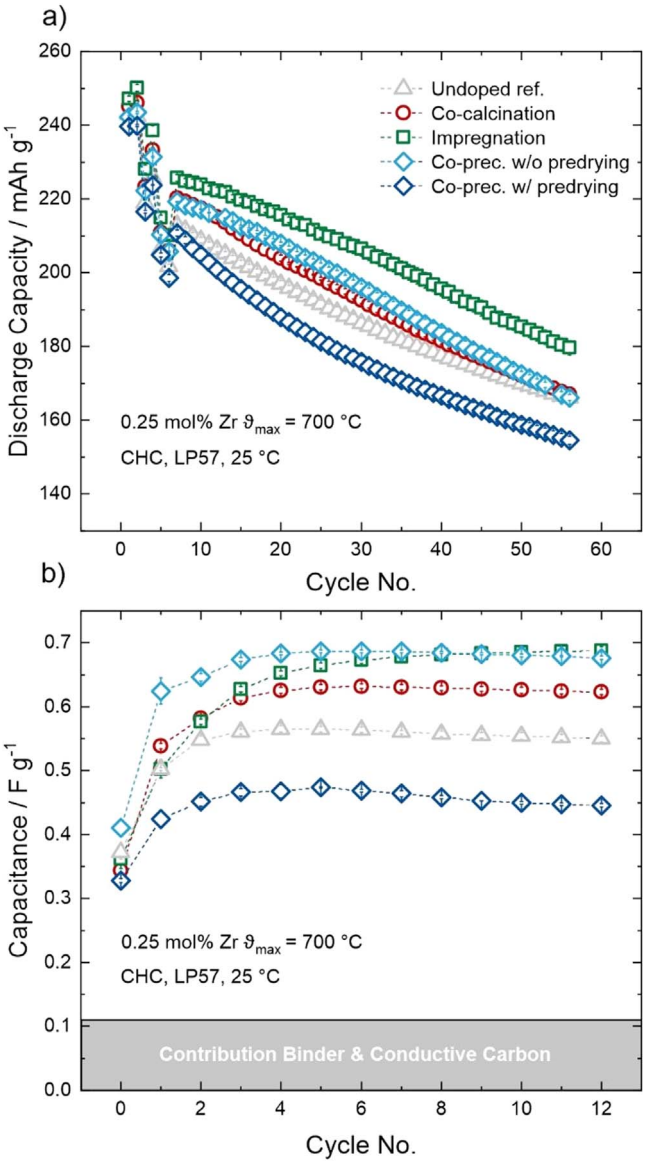

Figure 4. Electrochemical testing of Zr-doped LNO CAMs (calcined at 700 °C) in coin half-cells. (a) Specific discharge capacity in the two initial cycles at C/20, during a rate test (one cycle each at C/3, C/10, 1 C and 2 C) and upon C/3 cycling. (b) Specific capacitance evolution during C/10 cycling.

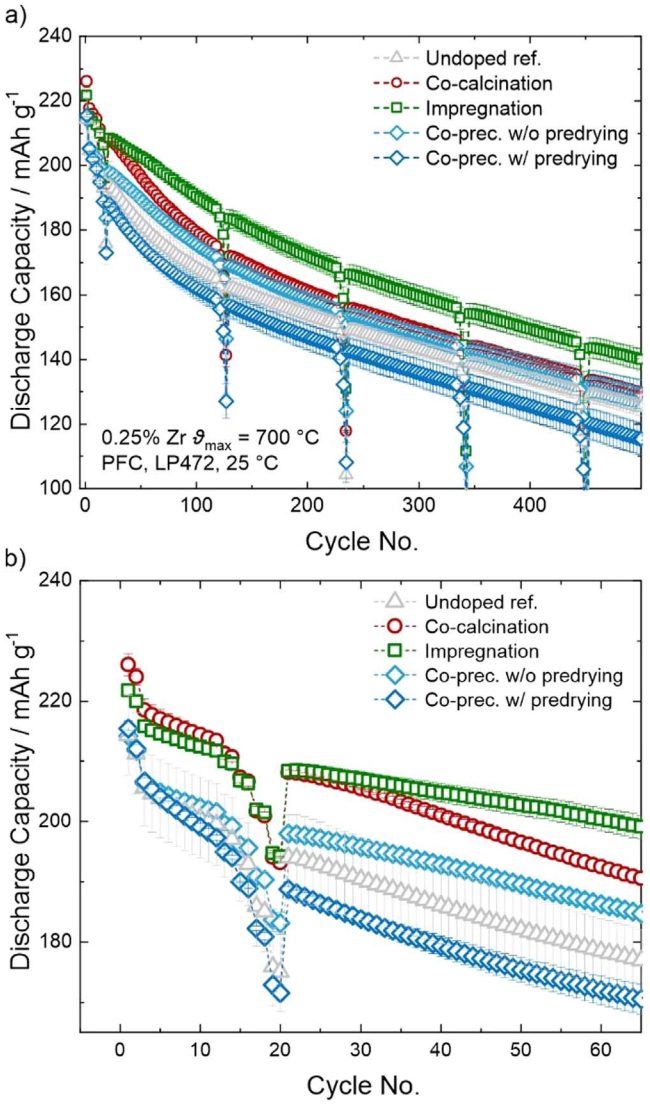

Figure 5. Electrochemical testing of Zr-doped LNO CAMs (calcined at 700 °C) in pouch full cells. Specific discharge capacity at C/3 with intermittent rate tests (C/3 charge and two cycles each at 0.5 C, 1 C, 2 C and 3 C discharge). (a) Long-term cycling performance and (b) first 50 cycles.

cells (referred to as PFC) during long-term cycling for each material. The overall performance is in the same order as for coin half-cells, except for the co-calcined LNO, where a slightly better cyclability is observed early in the testing, with 226 mAh g^{-1} at C/20 in the initial cycle and 208 mAh g^{-1} at C/3 after the rate test. The best performance is found for LNO obtained by pCAM impregnation (222 mAh g^{-1} in the initial cycle). The difference in capacity (capacity fade rate) between the materials remains rather constant from 150 cycles onward, as can be expected for uncoated CAM suffering mostly from continuous rocksalt-type phase formation and loss of Li inventory. While LNO obtained from pCAM impregnation, with a specific capacity of 180 mAh g^{-1} after 150 cycles and 140 mAh g^{-1} after 500 cycles, performs best in the later cycles, LNO from pre-dried, co-precipitated pCAM delivers specific capacities of only 215, 154 and 115 mAh g^{-1} in the 1st, 150th and 500th cycle, respectively. Figure 5b highlights the first 50 cycles, showing that, with the exception of slightly better performance of co-calcined LNO, the difference in cyclability between the materials is already established in the initial cycles (mostly due to the primary particle size), in agreement with both the coin cell data and capacitance trends discussed previously (see Fig. 4).

Lastly, for all CAMs calcined at 700 °C, the CO_2 evolution in the formation cycle was determined via DEMS. While the largest share of gas evolution during formation is due to solid electrolyte interphase (SEI) formation under release of ethylene at the anode, CO_2 generation is commonly observed at the cathode side.[72,90] In general, possible causes of CO_2 evolution are chemical oxidation of electrolyte by oxygen released from the CAM lattice during rocksalt-type layer formation at SOC > 80%,[91,92] electrochemical oxidation of carbonate electrolyte at potentials larger than ~4.6 V vs Li^+/Li[93] and decomposition of surface carbonate impurities.[94] In the initial cycle, and without overcharging, surface carbonate impurities often dominate the gas evolution, as the potential is too low for electrochemical oxidation and significant lattice oxygen release.[95] However, it is important to consider that a fair comparison of total gas evolution is thus only possible at similar SOC, i.e. specific charge capacity.[72,96,97] Therefore, Fig. 6 depicts both the total first-cycle CO_2 evolution and the charge capacity achieved with the DEMS cells. An exemplary gas evolution profile is shown for LNO from impregnated pCAM in Fig. S11. Note that delayed gas

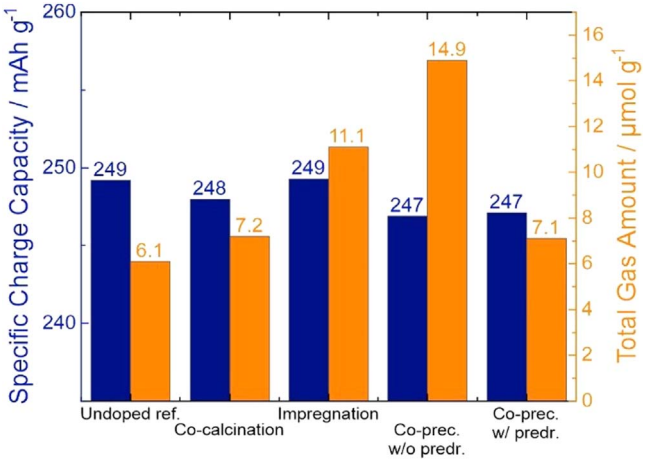

Figure 6. Comparison of total first-cycle gas evolution as determined by DEMS at similar specific charge capacity for LNO samples calcined at 700 °C.

evolution during discharge in the initial cycle is common for layered Ni-rich oxides.[98–100] Second-cycle gas evolution could not be quantified for all materials because of the low overall gassing of clean and dry-processed CAM at a regular cut-off potential of 4.3 vs Li^+/Li. Similarly, no molecular O_2 is detected, as it immediately reacts with the electrolyte upon release forming CO_2. The obtained gas amounts at this potential are in good agreement with previous reports.[69,92,95,99,101]

The observed larger total gas evolution for LNO obtained from non-pre-dried, co-precipitated pCAM is mostly a consequence of the higher amount of surface carbonates, as also reflected in the acid titration results shown in Table I. However, it should be noted that not all surface carbonates are decomposed to CO_2 in the initial cycle.[95,97] Given that an increased CO_2 amount is also observed for the LNO obtained from impregnated pCAM, the other material with smaller primary particles, a contribution of lower primary particle size, i.e. higher specific surface area, has to be considered too, since a larger surface for carbonate impurities and rocksalt-type layer formation is exposed to electrolyte, which has been demonstrated by correlation of capacitance measurements with gas evolution data.[69,101] These results demonstrate that even "advanced" characterization methods are affected by the doping process route and resulting primary particle size differences, as a mere comparison between doped and undoped material would lead to different results depending on the chosen route.

Conclusions

In this work, the relations between dopant, process route, primary particle size and electrochemical performance of LNO were investigated on the example of 0.25 mol% Zr^{4+} doping. A comparison of undoped LNO and doped LNO either from co-calcination, co-precipitation or impregnation revealed that, while all materials showed similar unit-cell parameters and off-stoichiometry, the primary particle size was greatly affected by the process route, yet not by the mere presence of dopant. The dopant distribution in precursors as well as within and between secondary LNO particles was examined. Zirconium enrichment was found at the grain boundaries, suggesting a crystal growth inhibition mechanism for the dopant, the extent of which is depending on the initial dopant localization during calcination, and explaining the role of the doping process route. As the primary particle size determines the electrochemical performance, the different process routes consequently also manifest in cyclability, which was demonstrated not only in coin half-cells but also by long-term cycling of pouch full cells. Finally, other properties such as specific capacitance and gas evolution during cycling were also shown to be affected by the doping process route. Impregnation resulted in the smallest primary particles and therefore best electrochemical performance. The obtained results highlight that when studying dopants in small, industrially relevant concentrations, the process route determines the outcome of the study and needs to be chosen carefully. The significance of the process route as a function of the dopant concentration remains to be studied, as higher concentrations may lead to more significant segregation/phase separation and lattice parameter changes.

Acknowledgments

Francois Fauth and the BL04-MSPD beamline team at the ALBA synchrotron are acknowledged for their support to the PXRD measurements. Marie Duffiet and Damian Goonetilleke from KIT are acknowledged for performing the PXRD measurements. Felix Riewald from BASF SE is acknowledged for insightful discussions. This work was partially supported by BASF SE. This project has received funding from the European Union's Horizon 2020 research and innovation programme under grant agreement no. 957189. The project is part of BATTERY 2030+, the large-scale European research initiative for inventing the sustainable batteries of the future.

Data Availability Statement

The data that support the findings of this study are available from the corresponding author upon reasonable request.

ORCID

Philipp Kurzhals https://orcid.org/0000-0002-7013-080X
Torsten Brezesinski https://orcid.org/0000-0002-4336-263X
Jürgen Janek https://orcid.org/0000-0002-9221-4756

References

1. A. Manthiram, *Nat. Commun.*, **11**, 1550 (2020).
2. U.-H. Kim et al., *Energy Environ. Sci.*, **11**, 1271 (2018).
3. C. S. Yoon, D.-W. Jun, S.-T. Myung, and Y.-K. Sun, *ACS Energy Lett.*, **2**, 1150 (2017).
4. M. Bianchini, M. Roca-Ayats, P. Hartmann, T. Brezesinski, and J. Janek, *Angew. Chem. Int. Ed.*, **58**, 10434 (2019).
5. P. Kurzhals, F. Riewald, M. Bianchini, H. Sommer, H. A. Gasteiger, and J. Janek, *J. Electrochem. Soc.*, **168**, 110518 (2021).
6. F. Riewald, P. Kurzhals, M. Bianchini, H. Sommer, J. Janek, and H. A. Gasteiger, *J. Electrochem. Soc.*, **169**, 020529 (2022).
7. Z. Xu, Z. Wang, X. Tan, H. Guo, W. Peng, X. Li, J. Wang, and G. Yan, *J. Electrochem. Soc.*, **169**, 090520 (2022).
8. H.-J. Noh, S. Youn, C. S. Yoon, and Y.-K. Sun, *J. Power Sources*, **233**, 121 (2013).
9. N. S. Luu, K.-Y. Park, and M. C. Hersam, *Acc. Mater. Res.*, **3**, 511 (2022).
10. H.-H. Sun and A. Manthiram, *Chem. Mater.*, **29**, 8486 (2017).
11. P. Mukherjee, P. Lu, N. Faenza, N. Pereira, G. Amatucci, G. Ceder, and F. Cosandey, *ACS Appl. Mater. Interfaces*, **13**, 17478 (2021).
12. J. Xu, E. Hu, D. Nordlund, A. Mehta, S. N. Ehrlich, X.-Q. Yang, and W. Tong, *ACS Appl. Mater. Interfaces*, **8**, 31677 (2016).
13. Z. Cui, X. Li, X. Bai, X. Ren, and X. Ou, *Energy Storage Mater.*, **57**, 14 (2023).
14. C. P. Grey and D. S. Hall, *Nat. Commun.*, **11**, 6279 (2020).
15. Z. Ahaliabadeh, X. Kong, E. Fedorovskaya, and T. Kallio, *J. Power Sources*, **540**, 231633 (2022).
16. J. Yan, H. Huang, J. Tong, W. Li, X. Liu, H. Zhang, H. Huang, and W. Zhou, *Interdiscip. Mater.*, **1**, 330 (2022).
17. K.-J. Park, H.-G. Jung, L.-Y. Kuo, P. Kaghazchi, C. S. Yoon, and Y.-K. Sun, *Adv. Energy Mater.*, **8**, 1801202 (2018).
18. H.-H. Ryu, S.-B. Lee, and Y.-K. Sun, *J. Solid State Electrochem.*, **26**, 2097 (2022).
19. Y. Levartovsky, X. Wu, C. Erk, S. Maiti, J. Grinblat, M. Talianker, and D. Aurbach, *Battery Supercaps*, **4**, 221 (2021).
20. H. H. Sun, U.-H. Kim, J.-H. Park, S.-W. Park, D.-H. Seo, A. Heller, C. B. Mullins, C. S. Yoon, and Y.-K. Sun, *Nat. Commun.*, **12**, 6552 (2021).
21. Y. Levartovsky, S. Kunnikuruvan, A. Chakraborty, S. Maiti, J. Grinblat, M. Talianker, D. T. Major, and D. Aurbach, *J. Electrochem. Soc.*, **168**, 060552 (2021).
22. X. Jia, M. Yan, Z. Zhou, X. Chen, C. Yao, D. Li, D. Chen, and Y. Chen, *Electrochim. Acta*, **254**, 50 (2017).
23. S. Liu, Z. Dang, D. Liu, C. Zhang, T. Huang, and A. Yu, *J. Power Sources*, **396**, 288 (2018).
24. Y. Ming et al., *ACS Appl. Mater. Interfaces*, **12**, 8146 (2020).
25. X. Tan, W. Peng, M. Wang, G. Luo, Z. Wang, G. Yan, H. Guo, Q. Li, and J. Wang, *Prog. Nat. Sci. Mater. Int.*, **33**, 108 (2023).

26. C. S. Yoon, M.-J. Choi, D.-W. Jun, Q. Zhang, P. Kaghazchi, K.-H. Kim, and Y.-K. Sun, *Chem. Mater.*, **30**, 1808 (2018).
27. L. Wang, G. Liu, X. Ding, C. Zhan, and X. Wang, *ACS Appl. Mater. Interfaces*, **11**, 33901 (2019).
28. Z. Huang, Z. Wang, X. Zheng, H. Guo, X. Li, Q. Jing, and Z. Yang, *Electrochim. Acta*, **182**, 795 (2015).
29. B. Zhang, L. Li, and J. Zheng, *J. Alloys Compd.*, **520**, 190 (2012).
30. A. L. Lipson et al., *ACS Appl. Mater. Interfaces*, **12**, 18512 (2020).
31. C. S. Yoon, U.-H. Kim, G.-T. Park, S. J. Kim, K.-H. Kim, J. Kim, and Y.-K. Sun, *ACS Energy Lett.*, **3**, 1634 (2018).
32. Y. Lu, M. Pang, S. Shi, Q. Ye, Z. Tian, and T. Wang, *Sci. Rep.*, **8**, 2981 (2018).
33. J. Cheng, L. Mu, C. Wang, Z. Yang, H. L. Xin, F. Lin, and K. A. Persson, *J. Mater. Chem. A*, **8**, 23293 (2020).
34. L. Mu et al., *Chem. Mater.*, **31**, 9769 (2019).
35. H. Li, P. Zhou, F. Liu, H. Li, F. Cheng, and J. Chen, *Chem. Sci.*, **10**, 1374 (2019).
36. L. Mu, W. H. Kan, C. Kuai, Z. Yang, L. Li, C.-J. Sun, S. Sainio, M. Avdeev, D. Nordlund, and F. Lin, *ACS Appl. Mater. Interfaces*, **12**, 12874 (2020).
37. A. Gomez-Martin, F. Reissig, L. Frankenstein, M. Heidbüchel, M. Winter, T. Placke, and R. Schmuch, *Adv. Energy Mater.*, **12**, 2103045 (2022).
38. M. Yi, W. Li, and A. Manthiram, *Chem. Mater.*, **34**, 629 (2022).
39. G. Li, X. Rao, W. Yao, M. Zeng, S. Zhong, and H. Cheng, *Ionics*, **28**, 1055 (2022).
40. R. Du, Y. Bi, W. Yang, Z. Peng, M. Liu, Y. Liu, B. Wu, B. Yang, F. Ding, and D. Wang, *Ceram. Int.*, **41**, 7133 (2015).
41. T. Chen, X. Li, H. Wang, X. Yan, L. Wang, B. Deng, W. Ge, and M. Qu, *J. Power Sources*, **374**, 1 (2018).
42. D. Kitsche, S. Schweidler, A. Mazilkin, H. Geßwein, F. Fauth, E. Suard, P. Hartmann, T. Brezesinski, J. Janek, and M. Bianchini, *Mater. Adv.*, **1**, 639 (2020).
43. B. Han, S. Xu, S. Zhao, G. Lin, Y. Feng, L. Chen, D. G. Ivey, P. Wang, and W. Wei, *ACS Appl. Mater. Interfaces*, **10**, 39599 (2018).
44. G.-H. Kang, K.-W. Lee, K. Kwon, and J. Song, *Metals*, **7**, 395 (2017).
45. F. Wu, N. Liu, L. Chen, N. Li, Y. Lu, D. Cao, M. Xu, Z. Wang, and Y. Su, *ACS Appl. Mater. Interfaces*, **13**, 24925 (2021).
46. C.-H. Jung et al., *J. Mater. Chem. A*, **9**, 17415 (2021).
47. Q. Li, Z. Li, S. Wu, Z. Wang, X. Liu, W. Li, N. Li, J. Wang, and W. Zhuang, *ACS Appl. Energy Mater.*, **3**, 11741 (2020).
48. Y. Shen, X. Yao, S. Wang, D. Zhang, D. Yin, L. Wang, and Y. Cheng, *ACS Appl. Mater. Interfaces*, **13**, 58871 (2021).
49. M. Dalkilic, A. Schmidt, T. D. Schladt, P. Axmann, M. Wohlfahrt-Mehrens, and M. Lindén, *J. Electrochem. Soc.*, **169**, 120501 (2022).
50. M. Dalkilic, A. Schmidt, T. D. Schladt, P. Axmann, M. Wohlfahrt-Mehrens, and M. Lindén, *J. Electrochem. Soc.*, **169**, 090504 (2022).
51. Y. Huang, J. Chen, J. Ni, H. Zhou, and X. Zhang, *J. Power Sources*, **188**, 538 (2009).
52. D. Goonetilleke, A. Mazilkin, D. Weber, Y. Ma, F. Fauth, J. Janek, T. Brezesinski, and M. Bianchini, *J. Mater. Chem. A*, **10**, 7841 (2022).
53. F. Schipper et al., *J. Mater. Chem. A*, **4**, 16073 (2016).
54. F. A. Susai et al., *Materials*, **14**, 2070 (2021).
55. I. H. Kwon, H. R. Park, and Y. Y. Song, *Russ. J. Electrochem.*, **49**, 221 (2013).
56. F. Schipper et al., *Adv. Energy Mater.*, **8**, 1701682 (2018).
57. T. R. Penki et al., *J. Solid State Electrochem.*, **25**, 1513 (2021).
58. D. Weber, J. Lin, A. Pokle, K. Volz, J. Janek, T. Brezesinski, and M. Bianchini, *J. Electrochem. Soc.*, **169**, 030540 (2022).
59. G.-T. Park et al., *Energy Environ. Sci.*, **14**, 6616 (2021).
60. S. Tubtimkuna, N. Phattharasupakun, P. Bunyanidhi, and M. Sawangphruk, *Adv. Mater. Technol.*, **7**, 2200436 (2022).
61. F. Reissig, M. A. Lange, L. Haneke, T. Placke, W. G. Zeier, M. Winter, R. Schmuch, and A. Gomez-Martin, *Chem. Sus. Chem.*, **15**, e202102220 (2022).
62. X. Li, K. Zhang, M. Wang, Y. Liu, M. Qu, W. Zhao, and J. Zheng, *Sustain. Energy Fuels*, **2**, 413 (2018).
63. S. Sivaprakash and S. B. Majumder, *J. Alloys Compd.*, **479**, 561 (2009).
64. Y. Kim, *Phys. Chem. Chem. Phys.*, **21**, 12505 (2019).
65. Q. Chen, C. Du, D. Qu, X. Zhang, and Z. Tang, *RSC Adv.*, **5**, 75248 (2015).
66. C.-S. Kim, K. M. Jeong, K. Kim, and C.-W. Yi, *Electrochim. Acta*, **155**, 431 (2015).
67. S. Oswald, F. Riewald, and H. A. Gasteiger, *J. Electrochem. Soc.*, **169**, 040552 (2022).
68. S. Oswald, D. Pritzl, M. Wetjen, and H. A. Gasteiger, *J. Electrochem. Soc.*, **167**, 100511 (2020).
69. S. Oswald, D. Pritzl, M. Wetjen, and H. A. Gasteiger, *J. Electrochem. Soc.*, **168**, 120501 (2021).
70. B. B. Berkes, A. Jozwiuk, H. Sommer, T. Brezesinski, and J. Janek, *Electrochem. Commun.*, **60**, 64 (2015).
71. B. B. Berkes, A. Jozwiuk, M. Vracar, H. Sommer, T. Brezesinski, and J. Janek, *Anal. Chem.*, **87**, 5878 (2015).
72. S. L. Dreyer, A. Kondrakov, J. Janek, and T. Brezesinski, *J. Mater. Res.*, **37**, 3146 (2022).
73. M. Bianchini, F. Fauth, P. Hartmann, T. Brezesinski, and J. Janek, *J. Mater. Chem. A*, **8**, 1808 (2020).
74. P. Kurzhals, F. Riewald, M. Bianchini, S. Ahmed, A. M. Kern, F. Walther, H. Sommer, K. Volz, and J. Janek, *J. Electrochem. Soc.*, **169**, 050526 (2022).
75. R. Wang, Z. Li, Z. Yang, M. Zhang, D. Zhang, and Y. Yan, *Ceram. Int.*, **47**, 1268 (2021).
76. J.-Z. Kong, H.-F. Zhai, C. Ren, G.-A. Tai, X.-Y. Yang, F. Zhou, H. Li, J.-X. Li, and Z. Tang, *J. Solid State Electrochem.*, **18**, 181 (2014).
77. J. Kim, H. Lee, H. Cha, M. Yoon, M. Park, and J. Cho, *Adv. Energy Mater.*, **8**, 1702028 (2018).
78. Y. Kim, H. Park, J. H. Warner, and A. Manthiram, *ACS Energy Lett.*, **6**, 941 (2021).
79. H. Li, S. Dey, and R. H. R. Castro, *Acta Mater.*, **150**, 394 (2018).
80. F. Liu and R. Kirchheim, *J. Cryst. Growth*, **264**, 385 (2004).
81. S. B. Seiffert, F. Riewald, R. B. Berk, and U. Karst, *Manuscript in Preparation*.
82. P. J. Sylvester and S. E. Jackson, *Elements*, **12**, 307 (2016).
83. T.-N. Kröger, S. Wiemers-Meyer, P. Harte, M. Winter, and S. Nowak, *Anal. Chem.*, **93**, 7532 (2021).
84. T.-N. Kröger, P. Harte, S. Klein, T. Beuse, M. Börner, M. Winter, S. Nowak, and S. Wiemers-Meyer, *J. Power Sources*, **527**, 231204 (2022).
85. T. Schwieters, M. Evertz, A. Fengler, M. Börner, T. Dagger, Y. Stenzel, P. Harte, M. Winter, and S. Nowak, *J. Power Sources*, **380**, 194 (2018).
86. S. Smetaczek, A. Wachter-Welzl, R. Wagner, D. Rettenwander, G. Amthauer, L. Andrejs, S. Taibl, A. Limbeck, and J. Fleig, *J. Mater. Chem. A*, **7**, 6818 (2019).
87. K. S. Ho, K. O. Lui, K. H. Lee, and W. T. Chan, *Spectrochim. Acta, Part B*, **89**, 30 (2013).
88. D. Mozhayeva and C. Engelhard, *J. Anal. At. Spectrom.*, **35**, 1740 (2020).
89. A. Liu, N. Phattharasupakun, M. M. E. Cormier, E. Zsoldos, N. Zhang, E. Lyle, P. Arab, M. Sawangphruk, and J. R. Dahn, *J. Electrochem. Soc.*, **168**, 070503 (2021).
90. B. Rowden and N. Garcia-Araez, *Energy Reports*, **6**, 10 (2020).
91. J. Wandt, A. T. S. Freiberg, A. Ogrodnik, and H. A. Gasteiger, *Mater. Today*, **21**, 825 (2018).
92. D. Streich, C. Erk, A. Guéguen, P. Müller, F.-F. Chesneau, and E. J. Berg, *J. Phys. Chem. C*, **121**, 13481 (2017).
93. R. Jung, M. Metzger, F. Maglia, C. Stinner, and H. A. Gasteiger, *J. Phys. Chem. Lett.*, **8**, 4820 (2017).
94. S. E. Renfrew and B. D. McCloskey, *J. Am. Chem. Soc.*, **139**, 17853 (2017).
95. T. Hatsukade, A. Schiele, P. Hartmann, T. Brezesinski, and J. Janek, *ACS Appl. Mater. Interfaces*, **10**, 38892 (2018).
96. S. L. Dreyer, K. R. Kretschmer, Đ. Tripković, A. Mazilkin, R. Chukwu, R. Azmi, P. Hartmann, M. Bianchini, T. Brezesinski, and J. Janek, *Adv. Mater. Interfaces*, **9**, 2101100 (2022).
97. F. Strauss, J. H. Teo, A. Schiele, T. Bartsch, T. Hatsukade, P. Hartmann, J. Janek, and T. Brezesinski, *ACS Appl. Mater. Interfaces*, **12**, 20462 (2020).
98. C. Misiewicz, R. Lundström, I. Ahmed, M. J. Lacey, W. R. Brant, and E. J. Berg, *J. Power Sources*, **554**, 232318 (2023).
99. L. de Biasi, A. Schiele, M. Roca-Ayats, G. Garcia, T. Brezesinski, P. Hartmann, and J. Janek, *ChemSusChem*, **12**, 2240 (2019).
100. R. Lundström and E. J. Berg, *J. Power Sources*, **485**, 229347 (2021).
101. S. Oswald, M. Bock, and H. A. Gasteiger, *J. Electrochem. Soc.*, **169**, 050501 (2022).